as for the plasma described by (7.59). The light penetrates only a very short distance into the metal and is almost entirely reflected. But when the frequency is increased into the domain where $\epsilon(\omega) > 0$, the metal suddenly can transmit light and its reflectivity changes drastically. This occurs typically in the ultraviolet and leads to the terminology "ultraviolet transparency of metals." Determination of the critical frequency gives information on the density or the effective mass of the conduction electrons.*

E. Index of Refraction and Absorption Coefficient of Liquid Water as a Function of Frequency

As an example of the overall frequency behavior of the real part of the index of refraction and the absorption coefficient of a real medium, we take the ubiquitous substance, water. Our intent is to give a broad view and to indicate the tremendous variations that are possible, rather than to discuss specific details. Accordingly, we show in Fig. 7.9, on a log-log plot with 20 decades in frequency and 11 decades in absorption, a compilation of the gross features of $n(\omega) = \text{Re} \sqrt{\mu\epsilon/\mu_0\epsilon_0}$ and $\alpha(\omega) = 2 \, \text{Im} \sqrt{\mu\epsilon} \, \omega$ for liquid water at NTP. The upper part of the graph shows the interesting, but not spectacular, behavior of $n(\omega)$. At very low frequencies, $n(\omega) \simeq 9$, a value arising from the partial orientation of the permanent dipole moments of the water molecules. Above 10^{10} Hz the curve falls relatively smoothly to the structure in the infrared. In the visible region, shown by the vertical dashed lines, $n(\omega) \simeq 1.34$, with little variation. Then in the ultraviolet there is more structure. Above 6×10^{15} Hz ($h\nu \simeq 25$ eV) there are no data on the real part of the index of refraction. The asymptotic approach to unity shown in the figure assumes (7.59).

Much more dramatic is the behavior of the absorption coefficient α. At frequencies below 10^8 Hz the absorption coefficient is extremely small. The data seem unreliable (two different sets are shown), probably because of variations in sample purity. As the frequency increases toward 10^{11} Hz, the absorption coefficient increases rapidly to $\alpha \simeq 10^4$ m^{-1}, corresponding to an attenuation length of 100 μm in liquid water. This is the well-known microwave absorption by water. It is the phenomenon (in moist air) that terminated the trend during World War II toward better and better resolution in radar by going to shorter and shorter wavelengths.

In the infrared region absorption bands associated with vibrational modes of the molecule and possibly oscillations of a molecule in the field of its neighbors cause the absorption to reach peak values of $\alpha \simeq 10^6$ m^{-1}. Then the absorption coefficient falls precipitously over $7\frac{1}{2}$ decades to a value of $\alpha < 3 \times 10^{-1}$ m^{-1} in a narrow frequency range between 4×10^{14} Hz and 8×10^{14} Hz. It then rises again by more than 8 decades by 2×10^{15} Hz. This is a dramatic absorption *window* in what we call the *visible region*. The extreme transparency of water here has its origins in the basic energy level structure of the atoms and molecules. The reader may meditate on the fundamental question of biological evolution on this water-soaked planet, of why animal eyes see the spectrum from red to

---

*See Chapter 4 of D. Pines, *Elementary Excitations in Solids*, W. A. Benjamin, New York (1963), for a discussion of these and other dielectric properties of metals in the optical and ultraviolet region. More generally, see F. Wooten, *Optical Properties of Solids*, Academic Press, New York (1972) and *Handbook of Optical Constants of Solids*, ed. E. D. Palik, Academic Press, Boston (1991).
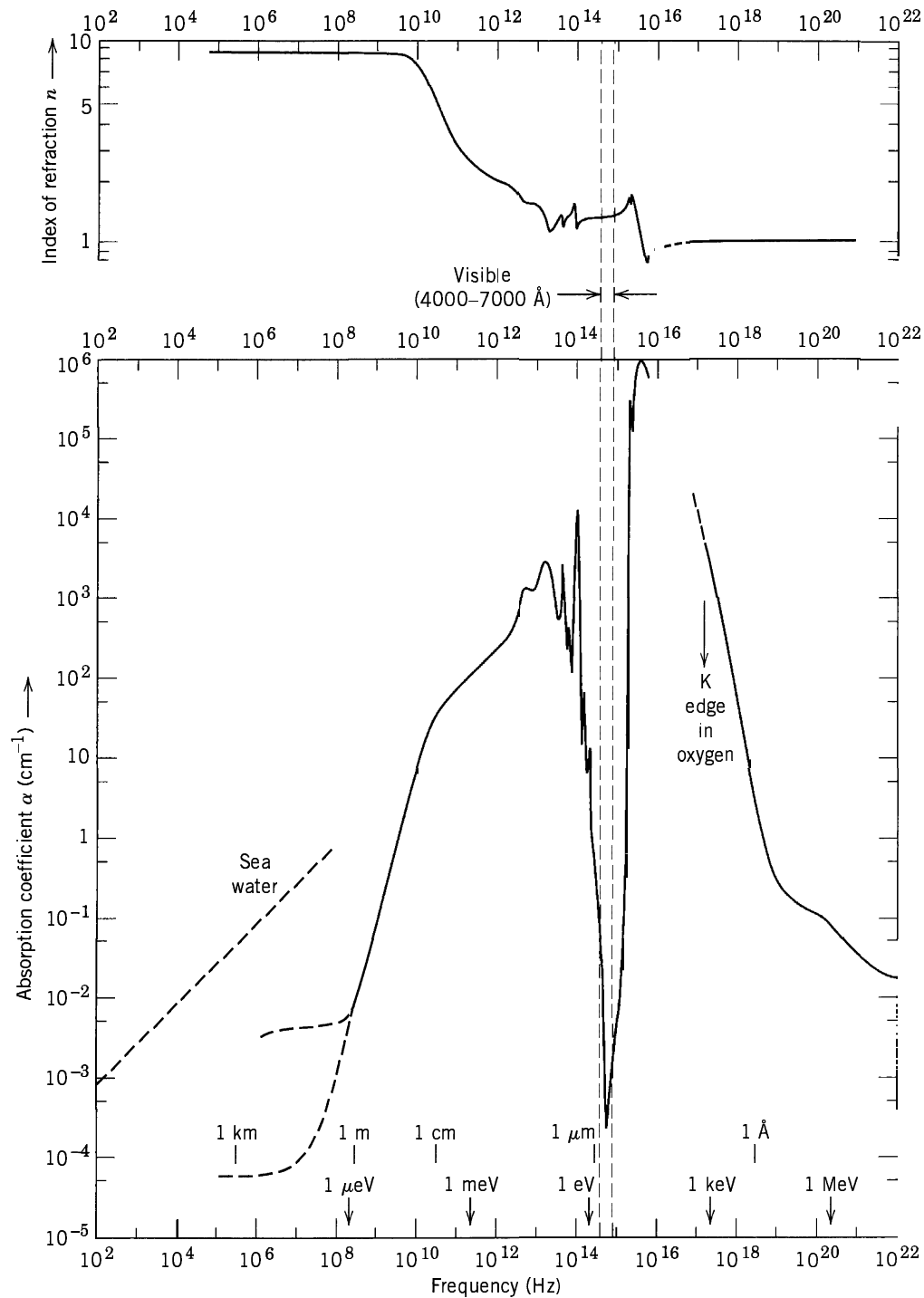
Figure 7.9 The index of refraction (top) and absorption coefficient (bottom) for liquid water as a function of linear frequency. Also shown as abscissas are an energy scale (arrows) and a wavelength scale (vertical lines). The visible region of the frequency spectrum is indicated by the vertical dashed lines. The absorption coefficient for seawater is indicated by the dashed diagonal line at the left. Note that the scales are logarithmic in both directions.

violet and of why the grass is green. Mother Nature has certainly exploited her window! In the very far ultraviolet the absorption has a peak value of $\alpha \simeq 1.1 \times 10^8$ m^{-1} at $\nu \simeq 5 \times 10^{15}$ Hz (21 eV). This is exactly at the plasmon energy $\hbar\omega_p$, corresponding to a collective excitation of all the electrons in the molecule. The attenuation is given in order of magnitude by (7.62). At higher frequencies data

are absent until the photoelectric effect, and then Compton scattering and other high-energy processes take over. There the nuclear physicists have studied the absorption in detail. The behavior is basically governed by the atomic properties and the density, not by the fact that the substance is water.

At the low-frequency end of the graph in Fig. 7.9 we have indicated the absorption coefficient of *seawater*. At low frequencies, seawater has an electrical conductivity $\sigma \simeq 4.4 \ \Omega^{-1} \ m^{-1}$. From (7.57) we find that below about 10^8 Hz $\alpha \simeq (2\mu_0\omega\sigma)^{1/2}$. The absorption coefficient is thus proportional to $\sqrt{\omega}$ and becomes very small at low frequencies. The line shown is $\alpha \ (m^{-1}) = 8.4 \times 10^{-3}\sqrt{\nu(Hz)}$. At 10^2 Hz, the attenuation length in seawater is $\alpha^{-1} \simeq 10$ meters. This means that 1% of the intensity at the surface will survive at 50 meters below the surface. If one had a large fleet of submarines scattered throughout the oceans of the world and wished to be able to send messages from a land base to the submerged vessels, one would be led to consider extremely low-frequency (ELF) communications. The existence of prominent resonances of the earth-ionosphere cavity in the range from 8 Hz to a few hundred hertz (see Section 8.9) makes that region of the frequency spectrum specially attractive, as does the reduced attenuation. With wavelengths of the order of 5×10^3 km, very large antennas are needed (still small compared to a wavelength!).*

7.6 Simplified Model of Propagation in the Ionosphere and Magnetosphere

The propagation of electromagnetic waves in the ionosphere is described in zeroth approximation by the dielectric constant (7.59), but the presence of the earth's magnetic field modifies the behavior significantly. The influence of a static external magnetic field is also present for many laboratory plasmas. To illustrate the influence of an external magnetic field, we consider the simple problem of a tenuous electronic plasma of uniform density with a strong, static, uniform, magnetic induction $\mathbf{B}_0$ and transverse waves propagating parallel to the direction of $\mathbf{B}_0$. (The more general problem of an arbitrary direction of propagation is contained in Problem 7.17.) If the amplitude of electronic motion is small and collisions are neglected, the equation of motion is approximately

$$m\ddot{\mathbf{x}} - e\mathbf{B}_0 \times \dot{\mathbf{x}} = -e\mathbf{E}e^{-i\omega t} \tag{7.63}$$

where the influence of the **B** field of the transverse wave has been neglected compared to the static induction $\mathbf{B}_0$ and the electronic charge has been written as $-e$. It is convenient to consider the transverse waves as circularly polarized. Thus we write

$$\mathbf{E} = (\boldsymbol{\epsilon}_1 \pm i\boldsymbol{\epsilon}_2)E \tag{7.64}$$

and a similar expression for **x**. Since the direction of $\mathbf{B}_0$ is taken orthogonal to $\boldsymbol{\epsilon}_1$ and $\boldsymbol{\epsilon}_2$, the cross product in (7.63) has components only in the direction $\boldsymbol{\epsilon}_1$ and

ELECTROMAGNETIC IMPULSE RESPONSE
OF TRIPLY-DISTILLED WATER

Judith E. K. Laurens and Kurt E. Oughstun

College of Engineering and Mathematics
University of Vermont
Burlington, VT 05405-0156

INTRODUCTION

As a pulse propagates through a linear dispersive, lossy medium, each spectral component propagates at its own characteristic phase velocity $v_p(\omega) = \omega/\beta(\omega)$ and is attenuated at a rate characterized by its attenuation coefficient $\alpha(\omega) = \Im\{\tilde{k}(\omega)\}$, where $\tilde{k}(\omega) = \beta(\omega) + i\alpha(\omega)$ is the complex wavenumber of a time-harmonic plane wave of angular frequency ω. The relative phases and amplitudes of the spectral components of the initial pulse then change by differing amounts as the propagation distance increases, giving rise to the observed distortion of the propagated pulse. The usual depiction of the dynamical pulse evolution relies upon the approximations associated with the group velocity description[1-4]; however, the accuracy of that approach breaks down as the pulse becomes either ultrashort or ultrawideband and so is inappropriate in this regime[5,6].

The correct description of ultrawideband pulse propagation in a linear, causally dispersive dielectric originated in 1914 with the classical analysis of Sommerfeld[7] and Brillouin[8,9] who used the then newly developed asymptotic method of steepest descents[10] to describe the dynamical evolution of the propagated field due to an input unit step-function modulated signal of constant carrier frequency in a single resonance Lorentz model dielectric. The modern asymptotic description[11-14] has shown the critical role that the precursor fields, originally introduced by Sommerfeld[7] and Brillouin[8,9], play in both the signal arrival and the resultant pulse distortion for ultrawideband fields as they propagate in a single resonance Lorentz medium. This modern asymptotic description is based on Olver's saddle point method[15], a generalization of the method of steepest descents, together with appropriate uniform asymptotic expansion techniques[14], and provides an accurate description of the entire dynamical field evolution in the mature dispersion regime. This modern description has shown that the precursor fields dominate the propagated field structure in dispersive, lossy dielectrics[16-20] in the mature dispersion regime and that they carry significant energy deeper into the lossy, dispersive medium[21] than that predicted by traditional analyses. These precursor

fields persist for noninstantaneous rise-time input pulses[5,6,14,22] provided that the initial rise-time (or fall-time) is on the order of or less than the characteristic medium relaxation time. Their potentially profound impact on health and safety studies is just beginning to be appreciated[23].

This asymptotic description is a canonical theory, the most fundamental problems involving the impulse response of the dispersive medium and the propagation of a unit step-function modulated signal through the medium. The theory has primarily considered the single resonance Lorentz model dielectric[5-9,11-14,21] and has only been extended to the double resonance Lorentz model in the special case when the two resonances have similar loss[24]; this extension has shown the formation of an additional precursor field that evolves between the Sommerfeld and Brillouin precursors[6,24]. In addition, numerical results for a single relaxation time Debye model dielectric[16-18] have shown the presence of a Brillouin precursor, but the absence of any Sommerfeld precursor in the propagated field structure due to an input ultrawideband microwave pulse. The present analysis provides an extension of these results to a causal model of the dielectric dispersion of triply-distilled H_2O whose orientational polarization dispersion is described by several relaxation times and whose electronic polarization dispersion contains several resonance lines with dissimilar loss coefficients[25].

The exact integral representation of the propagated plane wave field in the half-space $z \geq 0$ is given by[14]

$$A(z,t) = \frac{1}{2\pi} \int_C \tilde{f}(\omega) \exp\left\{\frac{z}{c}\phi(\omega,\theta)\right\} d\omega \quad , \tag{1}$$

where $\tilde{f}(\omega)$ is the temporal Fourier spectrum of the initial pulse $f(t) = A(0,t)$ at the plane $z = 0$. Here $A(z,t)$ represents any scalar component of the electric or magnetic field vector whose spectrum $\tilde{A}(z,\omega)$ satisfies the scalar Helmholtz equation

$$\left(\nabla^2 + \tilde{k}^2(\omega)\right)\tilde{A}(z,\omega) = 0 \quad . \tag{2}$$

The complex wavenumber appearing here is given by

$$\tilde{k}(\omega) = \omega n(\omega)/c \quad , \tag{3}$$

with $\beta(\omega) = \Re\left\{\tilde{k}(\omega)\right\}$ the plane wave propagation factor and $\alpha(\omega) = \Im\left\{\tilde{k}(\omega)\right\}$ the plane wave attenuation factor, where c denotes the speed of light in vacuum, and where $n(\omega) = \left[\mu\varepsilon(\omega)\right]^{1/2}$ is the complex index of refraction of the dispersive medium occupying the half-space $z \geq 0$ with relative magnetic permeability μ and complex-valued, relative dielectric permittivity $\varepsilon(\omega) = \varepsilon_r(\omega) + i\varepsilon_i(\omega)$. If $f(t) = 0$ for $t < 0$, then Eq. (1) is taken to be a Laplace representation for which the contour of integration C in the complex ω-plane is the Bromwich contour[14] that is given by the straight line $\omega = \omega' + ia$ with a being a real-valued constant that is greater than the abscissa of absolute convergence for the function $f(t)$, and where $\omega' \equiv \Re\{\omega\}$ varies from negative to positive infinity. The complex phase function $\phi(\omega,\theta)$ appearing in Eq. (1) is given by

$$\phi(\omega,\theta) = i\frac{c}{z}\left[\tilde{k}(\omega)z - \omega t\right] = i\omega[n(\omega) - \theta] \quad , \tag{4}$$

where

$$\theta = ct/z \tag{5}$$

is a dimensionless parameter that characterizes any given space-time point in the propagated field. The asymptotic theory provides a uniformly valid description of the temporal evolution of the field at any sufficiently large, fixed value of the propagation distance z .

A dielectric material of central importance to bioelectromagnetic effects is triply-distilled water[16-18,23], as it forms the base for many biological systems. Representative experimental data points for the real frequency dispersion of both the real index of refraction $n_r(\omega) = \Re\{n(\omega)\}$ and the absorption coefficient $\alpha(\omega) = (\omega/c)n_i(\omega)$ with $n_i(\omega) = \Im\{n(\omega)\}$ of triply-distilled water are illustrated in Fig. 1. The measured low frequency dependence of $n_r(\omega)$ for $0 \le \omega/2\pi \le 10^{13} Hz$ is characteristic of rotational polarization in polar dielectrics while the high frequency dependence observed for $\omega/2\pi > 10^{13} Hz$ is characteristic of resonance polarization in dielectrics[26]. The frequency dispersion due to rotational polarization is described here using the Rocard-Powles model[27], which is a first-order correction to the classic Debye model[28,29] of polar media, while the frequency dispersion due to resonance polarization is described here using the classical Lorentz oscillator model[30,31]. Both of these physical models are causal.

A composite Rocard-Powles-Lorentz model[25] with two relaxation times and four separate resonance frequencies that is appropriate for the observed frequency dispersion of the dielectric permittivity of triply-distilled water is given by

$$\varepsilon(\omega) = \varepsilon_\infty + \sum_{j=0,2}\frac{a_j}{\left(1 - i\omega\tau_j\right)\left(1 - i\omega\tau_{fj}\right)} - \sum_{j=11,13,15,17}\frac{b_j^2}{\omega^2 - \omega_j^2 + 2i\delta_j\omega} \quad . \tag{6}$$

Here τ_j is the macroscopic Debye relaxation time and τ_{fj} is the associated friction time in the Rocard-Powles model. In the infinitely large friction limit, each friction time vanishes and the first summation in Eq. (6) reduces to the expression for the dielectric permittivity in the Debye theory[25,28,29]. In the second summation over resonance polarization terms, each Lorentz model resonance line is characterized by the parameter triple $(\omega_j, b_j, \delta_j)$, where ω_j is the undamped resonance frequency, b_j the plasma frequency, and δ_j the phenomenological damping constant associated with the jth Lorentz oscillator type[25,30,31]. Finally, the quantity ε_∞ denotes the value of the dielectric permittivity in the limit as $\omega \to \infty$.

The medium parameters for the Rocard-Powles model component of Eq. (6) were fit to the data points first over the frequency domain $0 \le \omega/2\pi \le 10^{13} Hz$ using just the first three terms on the right-hand side of Eq. (6) with ε_∞ replaced by the parameter $\varepsilon_{\infty rot}$ which is appropriate for this model component[25]. The rms best fit result is depicted by the solid curves in Fig. 2 along with the associated parameter values. The dashed curves in the figure shows the rms best fit Debye model result $(\tau_{fj} = 0, j = 0,2)$ for

comparison. Notice that when $\omega > 1/\tau_2 \approx 6\pi \times 10^{12} Hz$, the theoretical Debye model absorption curve rapidly approaches a constant limiting value that is known as the Debye plateau[27]; the inadequacy of this model for all $\omega > 1/\tau_2$ is clearly evident.
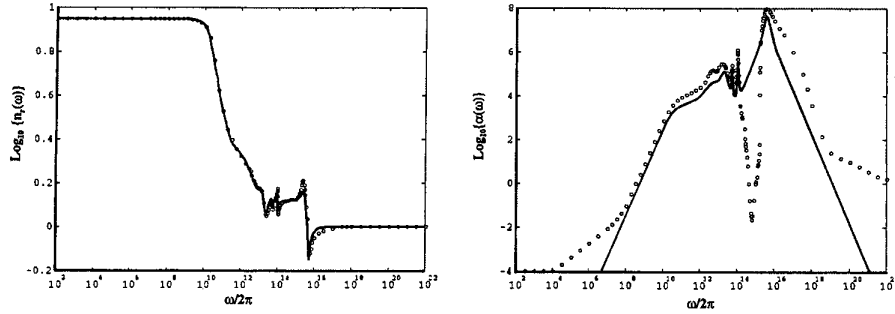

Figure 1. Experimental values (open circles) and optimized theoretical behavior (solid curves) of the frequency dispersion of the real index of refraction $n_r(\omega)$ and the absorption coefficient $\alpha(\omega)$, in units of m^{-1}, of triply-distilled water over the frequency domain from $\omega/2\pi = 1 \times 10^2 Hz$ to $\omega/2\pi = 1 \times 10^{22} Hz$. (Data supplied by the School of Aerospace Medicine, Armstrong Laboratory, Brooks Air Force Base).
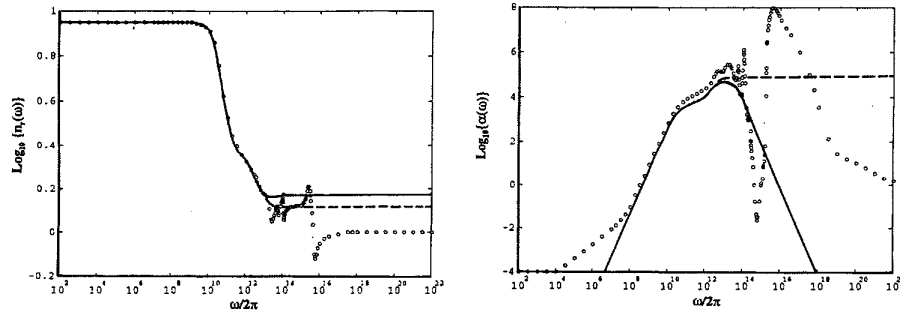

Figure 2. Experimental values (open circles) and rms best fit behavior of the frequency dispersion of the real index of refraction $n_r(\omega)$ and the absorption coefficient $\alpha(\omega)$ of triply-distilled water for the double relaxation time Rocard-Powles model (solid curves) with $\varepsilon_{\infty_{rot}} = 2.1$, $a_0 = 74.1$, $\tau_0 = (5.3/2\pi) \times 10^{-11} sec$, $\tau_{f0} = (2.9/2\pi) \times 10^{-13} sec$, $a_2 = 3.0$, $\tau_2 = (4.1/2\pi) \times 10^{-13} sec$, and $\tau_{f2} = (9.0/2\pi) \times 10^{-15} sec$, and for the double relaxation time Debye polarization model (dashed curves) with parameters $\varepsilon_{\infty_{rot}} = 1.7$, $a_0 = 74.7$, $\tau_0 = (5.3/2\pi) \times 10^{-11} sec$, $a_2 = 2.8$, and $\tau_2 = (3.0/2\pi) \times 10^{-13} sec$.

The medium parameters for the Lorentz model component of Eq.(6) were then fit to the data points by introducing each separate Lorentz model resonance line and determining its rms best fit parameters over a narrow frequency domain about that particular resonance frequency. Because the frequency dependence of each individual component of the full model extends over the entire frequency domain, the addition of each new resonance feature alters the rms fit of previously introduced features. As a consequence, the optimization procedure must be repeatedly applied so as to obtain the optimum rms fit for the entire model given in Eq.(6).

This was done for the Rocard-Powles model parameters whose values were used in Fig. 2. The final optimized result in the infrared to ultraviolet frequency domain is illustrated in Fig.3 where the location of each Lorentz model resonance frequency is indicated. Notice that the absorption due to the ultraviolet Lorentz resonance line at ω_{17} fills up the remaining half of the visible window in water. The optimized values of the Rocard-Powles-Lorentz model medium parameters appearing in Eq.(6) are given in Table 1. These parameter values are in good agreement with published results[32] for a simpler composite Debye-Lorentz model of the complex permittivity of water below $1THz$.
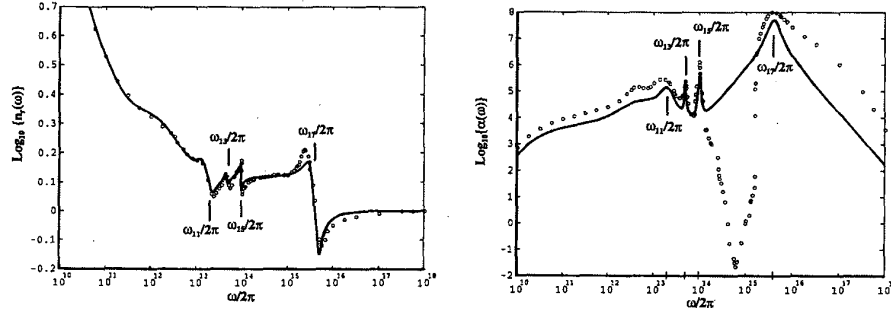

Figure 3. Experimental values (open circles) and optimized theoretical behavior (solid curves) of the frequency dispersion of the real index of refraction $n_r(\omega)$ and the absorption coefficient $\alpha(\omega)$ of triply-distilled water for the full Rocard-Powles-Lorentz polarization model with medium parameters as given in Table 1. The locations of the four Lorentz resonance frequencies are indicated in each diagram.

A comparison of the theoretical behavior and the experimental data of the real index of refraction and absorption for triply-distilled water over the entire frequency domain of interest is illustrated in Fig. 1. Notice that the experimental absorption data forms an upper bound to the theoretical curve over all but the visible region of the electromagnetic spectrum. Since the Rocard-Powles-Lorentz model (6) of the dielectric dispersion is strictly causal, it is then seen that the experimental absorption data for triply-distilled water is overestimated in both the low $(0 \leq \omega < 2\pi \times 10^8 Hz)$ and high $(\omega > 2\pi \times 10^{18} Hz)$ frequency domains. In its present form, Eq.(6) is seen to provide an accurate model of the dielectric dispersion of triply-distilled water from the static $(\omega = 0)$ through the infrared $(\omega \approx 2\pi \times 10^{14} Hz)$ region of the electromagnetic spectrum. The most notable shortfall of this model is the near complete loss of the visible window, which is nearly equally due to both the rotational and resonance portions of the model.

IMPULSE RESPONSE OF THE ROCARD-POWLES-LORENTZ MODEL OF THE DIELECTRIC DISPERSION OF TRIPLY-DISTILLED WATER

The integral representation of the impulse response of the model dielectric is obtained from Eq.(1) with $\tilde{f}(\omega) = 1$ as

$$A(z,t) = \frac{1}{2\pi} \int_C \exp\left\{\frac{z}{c}\phi(\omega,\theta)\right\} d\omega \qquad . \tag{7}$$

An exact evaluation of Eq. (7) may be achieved by application of Cauchy's residue theorem to that integral taken over the closed contour $C_0 = C + C_R$ if the integral over the semi-circular arc C_R at infinity vanishes. From the limiting behavior

$$\lim_{|\omega| \to \infty} \{n(\omega)\} = \sqrt{\varepsilon_\infty} \quad , \tag{8}$$

obtained from Eq. (6) for any value of $\arg(\omega)$, the integrand appearing in Eq.(7) takes on the limiting form

$$\exp\left\{\frac{z}{c}\phi(\omega,\theta)\right\} \to \exp\left\{\frac{z}{c}|\omega|\left[\left(-\sin\xi + i\cos\xi\right)\left(\varepsilon_\infty^{\frac{1}{2}} - \theta\right)\right]\right\} \tag{9}$$

as $|\omega| \to \infty$, where $\omega = |\omega|\exp(i\xi)$. If the inequality $\varepsilon_\infty^{\frac{1}{2}} - \theta > 0$ is satisfied, then the contour may be completed by taking C_R as the semi-circular arc in the upper-half plane since the integrand (9) goes to zero exponentially along C_R as its radius $|\omega| \to \infty$. Since the integrand in Eq.(7) has no poles in the upper-half plane, then the residue theorem yields the exact result

$$A(z,t) = 0 \quad , \quad \theta < \varepsilon_\infty^{\frac{1}{2}} \quad . \tag{10}$$

For $\theta > \varepsilon_\infty^{\frac{1}{2}}$ the integral representation (7) of the propagated field may be evaluated either numerically or by using asymptotic methods of analysis.

The complete precursor field structure that characterizes the electromagnetic impulse response of the Rocard-Powles-Lorentz model of the frequency dispersion of the dielectric permittivity of triply-distilled water, as given by Eq.(6) with the medium parameters listed in Table 1, is illustrated in the sequence of plots given in Fig. 4. These results were obtained using a numerical inverse Laplace transform algorithm[33] applied to the integral representation (7) at the fixed propagation distance $z = 6\pi \times 10^{-5}\,m$, which is sufficiently large to place the field evolution in the mature dispersion regime[11-14], and are displayed as a function of the dimensionless space-time parameter $\theta = ct/z$ which, at fixed z, is a dimensionless time parameter.

The overall structure of the propagated field evolution illustrated in Fig. 4(a) is quite similar to that obtained for either a single[11-14] or a double[13,24] resonance Lorentz model dielectric. The front of the field arrives at the speed of light in vacuum with an infinite instantaneous oscillation frequency that chirps down towards the upper end of the upper absorption band modeled in Eq.(6), and is referred to as a Sommerfeld precursor[20]. This is followed by a quasi-static field whose amplitude rapidly builds to a near-peak value that decays with the propagation distance only as $z^{-1/2}$, and is referred to as a Brillouin precursor[20]. However, the dynamical field evolution following the main peak in the Brillouin precursor, illustrated in Figs. 4(b,c,d), is quite different from that observed in previous studies for a Lorentz model medium. In addition, the peak value in the Brillouin precursor should appear[18,20] at or very near to the space-time point $\theta_0 \equiv n(0)$ which has the numerical value $n(0) \cong 8.90$ for triply-distilled water. Notice also in Fig. 4(a) that the oscillatory relaxation of the Brillouin precursor has been quenched. The detailed field evolution depicted in Fig. 4(b) for intermediate values of θ clearly exhibits the presence of interference

between two distinct frequency components that decay at essentially the same rate, while Fig. 4(c) shows the gradual buildup of a quasi-static field component. The detailed field evolution depicted in Fig. 4(d) for intermediate to large values of θ clearly shows the long time exponential decay of the impulse response in triply-distilled water. Each of these new and uniquely interesting features is explained in the remainder of this paper using asymptotic methods of analysis applied to the impulse response of the separate rotational and resonance portions of the composite Rocard-Powles-Lorentz model of the dielectric dispersion given in Eq.(6).
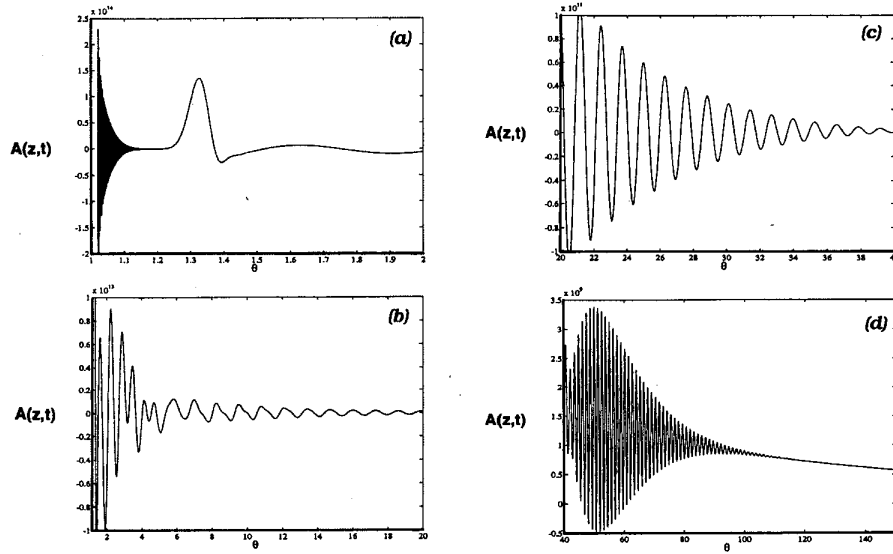

Figure 4. Dynamical evolution of the propagated field due to an input delta function pulse in the full Rocard-Powles-Lorentz model of triply-distilled water at the fixed propagation distance $z = 6\pi \times 10^{-5} m$ for small through large values of the space-time parameter $\theta = ct/z$.

ASYMPTOTIC DESCRIPTION OF THE IMPULSE RESPONSE OF A SINGLE RELAXATION TIME ROCARD-POWLES MODEL DIELECTRIC

Complex Phase Behavior in the Complex ω-Plane

The single relaxation time Rocard-Powles model of the orientational polarization response of a dielectric results in a complex-valued relative dielectric permittivity whose frequency dispersion is described by[25,27]

$$\varepsilon(\omega) = \varepsilon_{\infty_{rot}} + \frac{a_0}{(1 - i\omega\tau_0)(1 - i\omega\tau_{f0})} \quad , \tag{11}$$

where $\varepsilon_{\infty_{rot}} = \varepsilon(\infty)$, $\varepsilon_s = \varepsilon(0)$, $a_0 = \varepsilon_s - \varepsilon_{\infty_{rot}}$, τ_0 is the macroscopic relaxation time, and τ_{f0} is the friction time with $\tau_{f0} < \tau_0$. The corresponding complex index of refraction is then given by

249

$$n(\omega) = \left[\frac{\varepsilon_{\infty_{rot}} + a_0 - i\varepsilon_{\infty_{rot}}\left(\tau_0 + \tau_{f0}\right)\omega - \varepsilon_{\infty_{rot}}\tau_0\tau_{f0}\omega^2}{1 - i\left(\tau_0 + \tau_{f0}\right)\omega - \tau_0\tau_{f0}\omega^2} \right]^{\frac{1}{2}} \quad , \tag{12}$$

where $\mu/\mu_0 = 1$. For a single relaxation time Debye model dielectric, $\tau_{f0} = 0$.

The set of branch points of $n(\omega)$ are comprised of the pair of branch point singularities and branch point zeroes

$$\omega_{p1} = -\frac{i}{\tau_{f0}} \quad , \qquad \omega_{p2} = -\frac{i}{\tau_0} \quad , \tag{13a}$$

$$\omega_{z1,2} = -i\frac{\tau_0 + \tau_{f0}}{2\tau_0\tau_{f0}} \mp \frac{1}{2\tau_0\tau_{f0}}\left[4\frac{\varepsilon_{\infty_{rot}} + a_0}{\varepsilon_{\infty_{rot}}}\tau_0\tau_{f0} - \left(\tau_0 + \tau_{f0}\right)^2 \right]^{\frac{1}{2}} \quad , \tag{13b}$$

respectively. The two branch point zeroes coalesce on the negative imaginary axis when the friction time τ_{f0} equals the critical value

$$\tau_{f0}^c \equiv \tau_0 \left\{ \left(2\frac{\varepsilon_{\infty_{rot}} + a_0}{\varepsilon_{\infty_{rot}}} - 1 \right) - \sqrt{\left(2\frac{\varepsilon_{\infty_{rot}} + a_0}{\varepsilon_{\infty_{rot}}} - 1 \right)^2 - 1} \right\} \quad . \tag{14}$$

The branch cut $\left[\omega_{z2}, \omega_{p2}\right]$ associated with the relaxation time τ_0 is situated along the negative imaginary axis for $\tau_{f0} \le \tau_{f0}^c$. The branch cut $\left[\omega_{p1}, \omega_{z1}\right]$ that is associated with the friction time is located on the imaginary axis at $-i\infty$ when $\tau_{f0} = 0$ (in which limit the Debye model is obtained) and moves up the imaginary axis and approaches the lower end of the branch cut $\left[\omega_{z2}, \omega_{p2}\right]$ as τ_{f0} increases toward the critical value τ_{f0}^c. When $\tau_{f0} = \tau_{f0}^c$, the two branch point zeroes coalesce at the point $\omega_{z1} = \omega_{z2} = -i\left(\tau_0 + \tau_{f0}\right)/\left(\tau_0\tau_{f0}\right)$. Finally, when $\tau_{f0} > \tau_{f0}^c$ the branch point zeros move off the imaginary axis and are located at

$$\omega_{z1,2} = \frac{1}{2\tau_0\tau_{f0}}\left\{ \mp \sqrt{4\frac{\varepsilon_{\infty_{rot}} + a_0}{\varepsilon_{\infty_{rot}}}\tau_0\tau_{f0} - \left(\tau_0 + \tau_{f0}\right)^2} - i\left(\tau_0 + \tau_{f0}\right) \right\} \quad . \tag{15}$$

The branch cuts are now the line segments $\left[\omega_{p1}, \omega_{p2}\right]$ and $\left[\omega_{z1}, \omega_{z2}\right]$.

For the particular case of water with the Rocard-Powles model parameter values given in Fig.2, the branch points and their associated branch cuts are found to be situated along the imaginary axis. For notational simplicity the expressions for the branch point singularities and zeros in this case may be respectively expressed as

$$\omega_{p1,2} = -i\frac{\tau_p \pm c_p}{2\tau_m^2} \quad , \qquad \omega_{z1,2} = -i\frac{\tau_p \mp c_z}{2\tau_m^2} \quad , \tag{16}$$

where $\tau_p \equiv \tau_0 + \tau_{f0}$, $\tau_m^2 \equiv \tau_0\tau_{f0}$, $c_p \equiv \sqrt{\tau_p^2 - 4\tau_m^2}$, and $c_z \equiv \sqrt{\tau_p^2 - 4\tau_m^2\left(1 + a_0/\varepsilon_{\infty_{rot}}\right)}$ are all real-valued constants of the medium. This particular case is assumed

to hold throughout the remaining analysis. Other cases may be treated in a similar manner when the medium parameters warrant.

Saddle Point Dynamics of the Complex Phase Function

The saddle points of the complex phase function are located in the complex ω-plane at those values of ω that satisfy the saddle point equation $\phi'(\omega,\theta) = 0$, which results in the general expression

$$n(\omega) + \omega \frac{\partial n(\omega)}{\partial \omega} - \theta = 0 \quad , \tag{17}$$

so that the saddle point locations evolve with the space-time parameter θ. For the single relaxation time Rocard-Powles model dielectric, the saddle point equation becomes intractable and approximate solutions must be obtained in specific regions of the complex ω-plane[25].

For large $|\omega| \gg 1/\tau_m$, the complex index of refraction (12) may be approximated as

$$n(\omega) \approx \varepsilon_{\infty_{rot}}^{\frac{1}{2}} - \frac{a_0}{2\varepsilon_{\infty_{rot}}^{\frac{1}{2}} \tau_m^2 \omega\left(\omega + i\tau_p/\tau_m^2\right)} \quad . \tag{18}$$

With this substitution the saddle point equation (17) yields the pair of approximate solutions

$$\omega_{SP_D}^{\pm}(\theta) \approx \pm \left[\frac{a_0}{2\varepsilon_{\infty_{rot}}^{\frac{1}{2}} \tau_m^2\left(\theta - \varepsilon_{\infty_{rot}}^{\frac{1}{2}}\right)} \right]^{\frac{1}{2}} - i\frac{\tau_p}{\tau_m^2} \quad , \tag{19}$$

which are found[25] to be accurate for all $\theta \geq \sqrt{\varepsilon_{\infty_{rot}}}$. Because this pair of distant saddle points remain in the lower-half plane below the branch cut $[\omega_{z2}, \omega_{p2}]$, they are inaccessible and provide no contribution to the asymptotic behavior of the propagated field.

For small $|\omega| \ll |\omega_{p2}|$, the complex index of refraction (12) may be approximated by the quadratic expression[25]

$$n(\omega) \approx \frac{a_0\tau_m^2}{2\varepsilon_s^{\frac{1}{2}}}\left[1 - \frac{\tau_p^2}{4\varepsilon_s\tau_m^2}\left(\varepsilon_{\infty_{rot}} + 3\varepsilon_s\right)\right]\omega^2 + i\frac{a_0\tau_p}{2\varepsilon_s^{\frac{1}{2}}}\omega + \varepsilon_s^{\frac{1}{2}} \quad . \tag{20}$$

With this substitution the saddle point equation (17) yields the roots

$$\omega^{\pm}(\theta) \approx \frac{2\varepsilon_s^{\frac{1}{2}}}{3a_0\tau_m^2\left[1 - \frac{\tau_p^2}{4\varepsilon_s\tau_m^2}\left(\varepsilon_{\infty_{rot}} + 3\varepsilon_s\right)\right]}$$

$$\left\{ -i\frac{a_0\tau_p}{2\varepsilon_s^{\frac{1}{2}}} \pm \sqrt{\frac{3a_0\tau_m^2}{2\varepsilon_s^{\frac{1}{2}}}\left[1 - \frac{\tau_p^2}{4\varepsilon_s\tau_m^2}\left(\varepsilon_{\infty_{rot}} + 3\varepsilon_s\right)\right]\left(\theta - \theta_{RP}\right)} \right\} \quad , \tag{21}$$
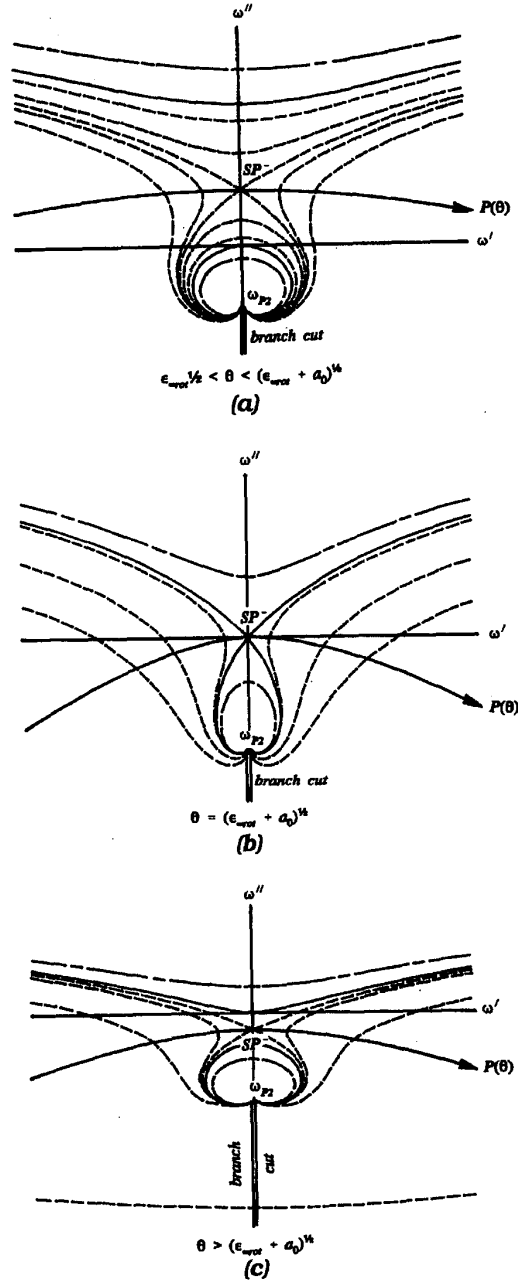
251

Figure 5. Topography of the isotimic contours of $X(\omega,\theta) = \Re\{\phi(\omega,\theta)\}$ in the complex ω-plane for a single relaxation time Rocard-Powles model dielectric with $\tau_{f0} < \tau_{f0}^c$ for several fixed, increasing values of the space-time parameter $\theta = ct/z$. The contour $P(\theta)$ is an Olver-type path with respect to the dominant saddle point at each value of θ depicted.

where

$$\theta_{RP} = \varepsilon_s^{1/2} \left[1 + \frac{a_0}{6\varepsilon_s \dfrac{\tau_m^2}{\tau_p^2} - \dfrac{3}{2}\left(\varepsilon_{\infty_{rot}} + \varepsilon_s\right)} \right] \quad .$$

(22)

The required inequality $\left|\omega^{\pm}(\theta)\right| \ll \left|\omega_{p2}\right|$ is not satisfied for $\theta \le \theta_{RP}$ and so neither root given in Eq.(21) yields a saddle point in that space-time domain. For $\theta > \theta_{RP}$ only the downward moving root $\omega^-(\theta)$ satisfies the required inequality, and so one obtains a single saddle point solution $\omega_{SP}^-(\theta) = \omega^-(\theta)$ for which the approximation given in Eq.(21) is valid over the space-time domain

$$\theta_{RP} < \theta < \varepsilon_s^{1/2} + \frac{a_0 \tau_p^2}{6\varepsilon_s^{1/2}\tau_m^2 \left[1 - \dfrac{\tau_p^2}{4\varepsilon_s \tau_m^2}\left(\varepsilon_{\infty_{rot}} + 3\varepsilon_s\right) \right]} \quad .$$

(23)

For the Rocard-Powles medium parameters given in Fig.2, this inequality becomes $7 < \theta < 10.77$, which agrees with the results of numerical studies[25]. The dynamical evolution of the saddle point location $\omega_{SP}^-(\theta)$ is illustrated in Fig. 5 over the space-time domain $\theta \ge \sqrt{\varepsilon_{\infty_{rot}}}$. At $\theta = \sqrt{\varepsilon_{\infty_{rot}}}$ this first-order saddle point is located in the upper-half plane along the imaginary axis and moves down the imaginary axis as θ increases, as seen in Fig. 5(a). At $\theta = n(0) = \sqrt{\varepsilon_{\infty_{rot}} + a_0}$ this saddle point crosses the origin, as seen in Fig. 5(b), and it approaches the branch point ω_{p2} in the limit as $\theta \to \infty$, as seen in Fig. 5(c). Similar behavior for this near saddle point is obtained for the single relaxation time Debye model dielectric[25].

Impulse Response of the Rocard-Powles Model Dielectric

The asymptotic description of the propagated field due to a delta function input in a single relaxation time Rocard-Powles model dielectric over the space-time domain $\theta > \varepsilon_{\infty_{rot}}^{1/2}$ is obtained through application of Olver's theorem[15] to the integral representation (7) when the contour C is deformed to an Olver-type path $P(\theta)$ with respect to the dominant, accessible saddle point SP^- with location $\omega_{SP}^-(\theta)$, as depicted in Fig. 5, with the result[14]

$$A(z,t) \sim \Re\left\{ \left[-\frac{c}{2\pi z \phi''\left(\omega_{SP}^-,\theta\right)} \right]^{1/2} e^{\frac{z}{c}\phi\left(\omega_{SP}^-,\theta\right)} \right\} \quad , \quad \theta > \varepsilon_{\infty_{rot}}^{1/2} \quad ,$$

(24)

as $z \to \infty$. Numerical and asymptotic calculations of the impulse response of the Rocard-Powles model dielectric whose medium parameters are given in Fig.2 at a fixed propagation distance of $z = 0.25m$ are essentially identical over the entire θ-domain of interest and are both illustrated by

the solid curve in Fig. 6. The observed dynamical field evolution is completely explained by the saddle point dynamics illustrated in Fig. 5 which describe a nonoscillatory field whose amplitude first increases over the space-time domain $1.77 \leq \theta < 8.89$ and reaches a maximum value at $\theta = n(0) = \sqrt{\varepsilon_s} = 8.89$ when the saddle point crosses the origin, at which space-time point the propagated field has no exponential decay and only decreases algebraically as $z^{-\frac{1}{2}}$, and whose amplitude then decreases for increasing $\theta > 8.89$ as the saddle point moves into the lower-half plane and approaches the branch point singularity at ω_{p2}. For comparison, the numerically determined impulse response of the corresponding single relaxation time Debye model dielectric is depicted by the dashed curve in Fig.6. The observed close agreement is a simple consequence of the similarity of the dominant saddle point dynamics for each medium model[25]. The identification of this temporally transient field structure as a Brillouin precursor follows from the analysis presented in Ref. 20. Although the Debye and Rocard-Powles models predict nearly identical Brillouin precursors, both of which are in approximate qualitative agreement with the Brillouin precursor exhibited in the impulse response of the complete dielectric permittivity model of water given in Fig. 4(a), they occur at a space-time point θ that differs substantially from that obtained with the complete model.
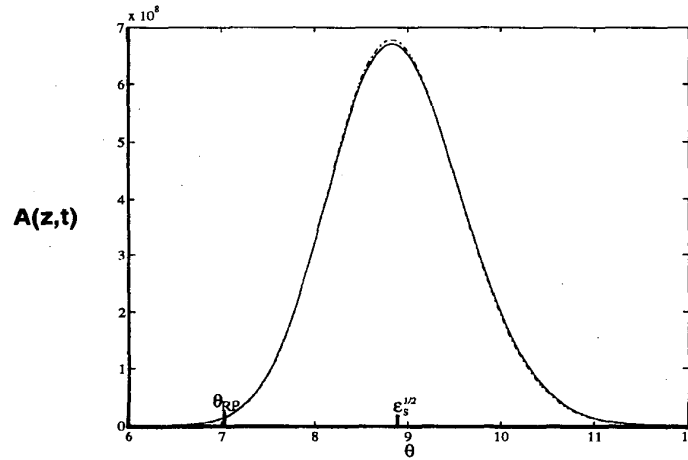

Figure 6. Dynamical field evolution due to an input delta function pulse at the fixed propagation distance $z = 0.25m$ over the space-time domain $\theta > \varepsilon_{\infty_{rot}}^{\frac{1}{2}}$ in the single relaxation time Debye (dashed curve) and Rocard-Powles (solid curve) models of the dielectric dispersion of triply-distilled water, where $\varepsilon_s^{\frac{1}{2}} = 8.89$ for both models.

ASYMPTOTIC DESCRIPTION OF THE IMPULSE RESPONSE OF A MULTIPLE RESONANCE LORENTZ MODEL DIELECTRIC

Complex Phase Behavior in the Complex ω-Plane

The Lorentz model for the resonance polarization response of a dielectric whose frequency dispersion is given by the second summation appearing in Eq.(2.1) results in the complex index of refraction

254

$$n(\omega) = \left[\varepsilon_\infty - \frac{b_{11}^2}{\omega^2 - \omega_{11}^2 + i2\delta_{11}\omega} - \frac{b_{13}^2}{\omega^2 - \omega_{13}^2 + i2\delta_{13}\omega} - \frac{b_{15}^2}{\omega^2 - \omega_{15}^2 + i2\delta_{15}\omega} - \frac{b_{17}^2}{\omega^2 - \omega_{17}^2 + i2\delta_{17}\omega} \right]^{\frac{1}{2}},$$

(25)

where $\mu/\mu_0 = 1$, and where ε_∞ is the limiting value of the dielectric permittivity as $\omega \to \infty$. These four Lorentz lines with the medium parameter values given in Table 1, which include the two resonance lines ω_{11} and ω_{13} in the far infrared, the single resonance line ω_{15} in the near infrared, and the single resonance line ω_{17} in the near ultraviolet regions of the electromagnetic spectrum, provide a fairly complete description of the medium response due to the prominent resonance features appearing in the frequency dispersion of triply-distilled water.

The branch point singularities of $n(\omega)$ are given by the set of relations

$$\omega_{j_p}^\pm = \pm\left(\omega_j^2 - \delta_j^2\right)^{\frac{1}{2}} - i\delta_j \qquad , \; j = 11,13,15,17 \quad,$$

(26)

while the locations of the branch point zeroes of the multiple resonance Lorentz model medium are given by the zeroes of the argument of the square root expression appearing in Eq.(25) and are denoted by $\omega_{j_z}^\pm$, $j = 11,13,15,17$. The branch cuts are taken as the set of line segments $\left[\omega_{j_z}^-, \omega_{j_p}^-\right]$ and $\left[\omega_{j_p}^+, \omega_{j_z}^+\right]$, $j = 11,13,15,17$, that are pair-wise symmetrically located about the imaginary axis, as seen in Fig. 7.

Saddle Point Dynamics of the Complex Phase Function

The saddle point dynamics for the multiple resonance Lorentz medium considered here are obtained from Eq.(17) with the complex index of refraction (25). This results in a 32nd-order polynomial equation in ω which yields 16 saddle points; the analytical solution of this equation is intractable so that numerical solutions must be relied upon.

The numerically determined paths followed by the 16 saddle points of the four resonance Lorentz model for triply-distilled water in the complex ω-plane over the space-time domain $\theta \geq \sqrt{\varepsilon_\infty}$ are presented in Fig. 7. Part (a) of that figure depicts a region of the plane that is appropriate for the saddle points that evolve in a region removed from the origin, while part (b) depicts a region that is appropriate for the saddle points that evolve in a region about the origin. The direction that each saddle point $\omega_{SP_j}(\theta)$ moves along its path as θ increases is indicated by the arrowhead along that path. Notice that the two weak resonance lines ω_{11} and ω_{13} in the far infrared region create an extremely complicated motion of the saddle points in the region about the origin and that this, in turn, will result in a corresponding intricate behavior in the dynamical evolution of the propagated field. The behavior of $X\left(\omega_{SP_j}, \theta\right) = \Re\left\{\phi\left(\omega_{SP_j}, \theta\right)\right\}$ at each saddle point for $\theta \geq \sqrt{\varepsilon_\infty}$ is illustrated in Fig. 8. Part (a) presents the overall behavior of each function $X\left(\omega_{SP_j}(\theta), \theta\right)$, while part (b) presents a detailed view of the significant order and dominance changes that occur at various critical values of θ. In order to unambiguously establish both the dominance and the accessibility of each of the saddle points over the

255

entire space-time domain $\theta \geq \sqrt{\varepsilon_\infty}$, it is necessary to consider the general topography of the isotimic contours of $X(\omega,\theta)$ in the complex ω -plane at each critical value of θ that marks a change in the order, the dominance, or the accessibility of any of the relevant saddle points, as determined from Fig. 8.
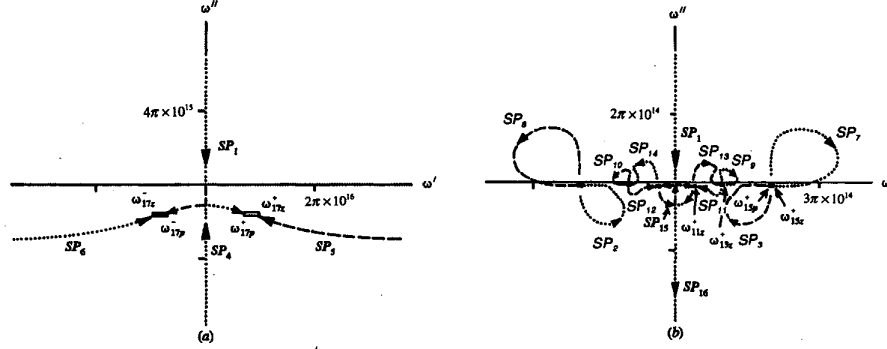

Figure 7. Saddle point trajectories in the complex ω-plane as a function of the space-time parameter $\theta \geq \varepsilon_\infty^{1/2}$ for the four resonance Lorentz model dielectric with parameters appropriate for triply-distilled water as given in Table 1. The branch cuts of $\phi(\omega,\theta)$ are indicated by the double line segments, and the arrowheads indicate the direction that a particular saddle point moves as θ increases.
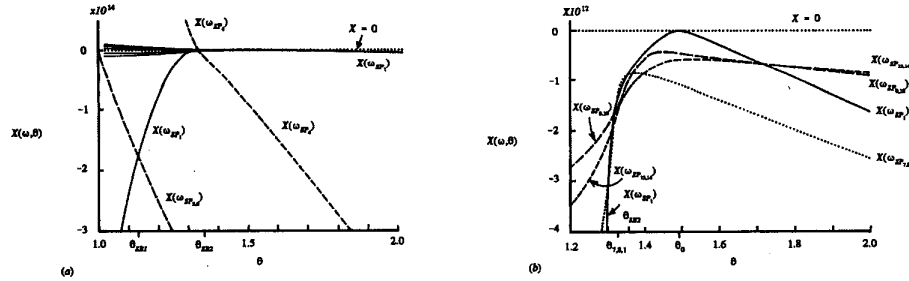

Figure 8. Behavior of $X\left(\omega_{SP_j},\theta\right) = \Re\left\{\phi\left(\omega_{SP_j},\theta\right)\right\}$ as a function of the space-time parameter $\theta \geq \varepsilon_\infty^{1/2}$ at the saddle points of the four resonance Lorentz model dielectric with parameters appropriate for triply-distilled water as given in Table 1.

The topography of the isotimic contours of $X(\omega,\theta)$ illustrated in Fig. 9(a) shows that the distant saddle point pair $SP_{5,6}$ is dominant and accessible by an Olver-type path $P(\theta)$ over the space-time domain $\varepsilon_\infty^{1/2} \leq \theta < \theta_{SB_1}$ and determines the initial behavior of the propagated field. At $\theta = \varepsilon_\infty^{1/2}$ this distant saddle point pair is located at $\pm\infty - i2\delta_{17}$ and from there moves in and approaches the respective branch point zeroes $\omega_{17_z}^\pm$ in the limit as $\theta \to \infty$.

When $\theta = \theta_{SB_1} \cong 1.133$, the distant saddle point pair $SP_{5,6}$ and the near saddle point SP_1 are of equal dominance, as seen in Fig. 9(b). The near

saddle point SP_1 moves down the positive imaginary axis and remains the dominant accessible saddle point over the space-time interval $\theta_{SB_1} < \theta < \theta_{7,1}$ with $\theta_{7,1} \cong 1.3235$, as illustrated in Fig. 10. This near saddle point continues to move down the imaginary axis as θ increases and crosses the origin at $\theta = \theta_0 = 1.49$. Notice that the pair of saddle points $SP_{7,8}$ become dominant over the near saddle point SP_1 at $\theta = \theta_{1,7} \cong 1.303$ but are inaccessible because there is no Olver-type path with respect to them.
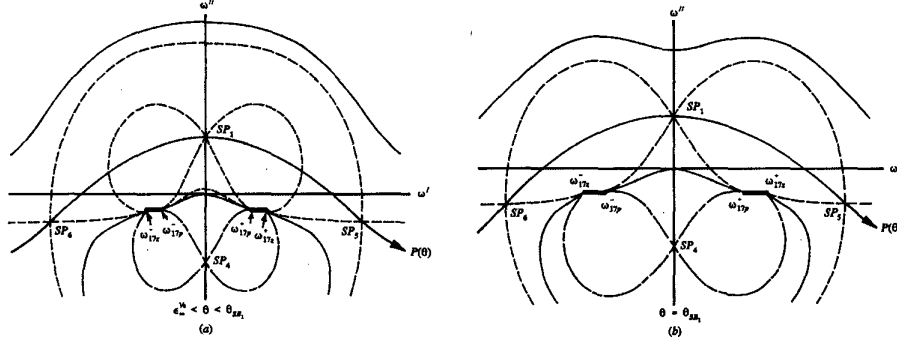

Figure 9. Topography of the isotimic contours of $X(\omega,\theta) = \Re\{\phi(\omega,\theta)\}$ in the complex ω-plane for large $|\omega|$ for the four resonance Lorentz model dielectric with parameters appropriate for triply-distilled water as given in Table 1.
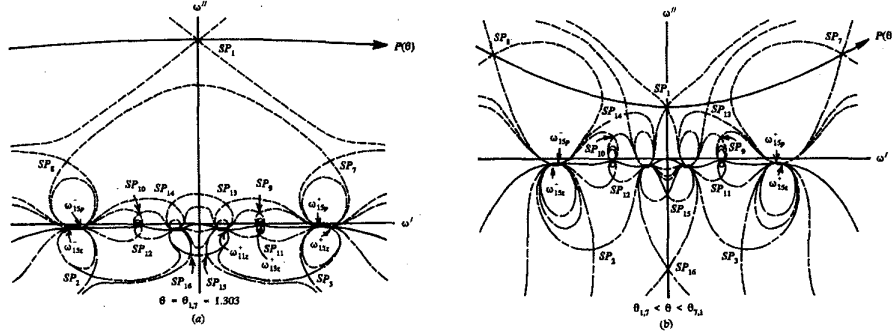

Figure 10. Topography of the isotimic contours of $X(\omega,\theta) = \Re\{\phi(\omega,\theta)\}$ in the complex ω-plane for small $|\omega|$ for the four resonance Lorentz model dielectric with parameters appropriate for triply-distilled water as given in Table 1.

When $\theta = \theta_{7,1} \cong 1.3235$, the saddle point pair $SP_{7,8}$ and the near saddle point SP_1 are again of equal dominance and this saddle point pair $SP_{7,8}$ is now accessible, as seen in Fig. 11(a). Notice that the saddle point pair $SP_{13,14}$ is also accessible at this space-time point, and the Olver-type path $P(\theta)$ with respect to the equally dominant saddle points SP_1 and $SP_{7,8}$ has been chosen so as to pass through these less dominant saddle points. The saddle point pair $SP_{7,8}$ is dominant and accessible over the short space-time interval $\theta_{7,1} < \theta < \theta_{SB_2}$, and the near saddle point SP_1 regains its dominance at $\theta = \theta_{SB_2} \cong 1.359$ and remains dominant and accessible over

257

the space-time interval $\theta_{SB_2} < \theta < \theta_1$, where the two first-order saddle points SP_1 and SP_{15} coalesce into a single second-order saddle point along the negative imaginary axis when $\theta = \theta_1 \cong 1.51$. These two first-order near saddle points then separate and symmetrically move off into the lower-half of the complex ω -plane for $\theta > \theta_1$, as seen in Fig. 11(b), approaching the innermost branch points $\omega_{11_p}^\pm$ in the limit as $\theta \to \infty$, and are the dominant, accessible saddle points over the space-time interval $\theta_1 < \theta < \theta_{9,1}$. Changes in dominance from the saddle point pair $SP_{1,15}$ to the saddle point pair $SP_{9,10}$ at $\theta = \theta_{9,1} \cong 1.71$ and then from that saddle point pair to the saddle point pair $SP_{13,14}$ at $\theta = \theta_{13,9} \cong 1.73$ establish the final set of dominance changes that occur. The accessible saddle point pair $SP_{13,14}$ remains dominant for all $\theta > \theta_{13,9}$ and approaches the branch points $\omega_{13_p}^\pm$ in the limit as $\theta \to \infty$. Notice that the saddle point pair $SP_{9,10}$ also remains accessible and is just barely dominated by the saddle point pair $SP_{13,14}$ for all $\theta > \theta_{13,9}$, that is, $X(\omega_{13,14},\theta) \cong X(\omega_{9,10},\theta)$ with $X(\omega_{13,14},\theta) < X(\omega_{9,10},\theta)$ over this entire space-time interval, and that this saddle point pair approaches the branch points $\omega_{13_z}^\pm$ in the limit as $\theta \to \infty$, as seen in Fig. 11(b).
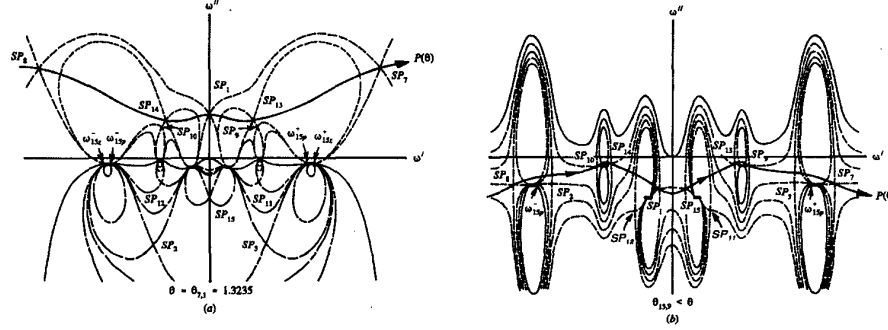

Figure 11. Topography of the isotimic contours of $X(\omega,\theta) = \Re\{\phi(\omega,\theta)\}$ in the complex ω-plane for small $|\omega|$ for the four resonance Lorentz model dielectric with parameters appropriate for triply-distilled water as given in Table 1.

Impulse Response of the Four Resonance Lorentz Model Dielectric

The nonuniform asymptotic description of the propagated field due to a delta function input in a four resonance Lorentz model dielectric over the space-time domain $\theta > \varepsilon_\infty^{1/2}$ is obtained through a straightforward application of Olver's theorem[15] to the integral representation given in Eq.(7) when the contour C is deformed to an Olver-type path $P(\theta)$ with respect to the dominant, accessible saddle points of $\phi(\omega,\theta) = i\omega(n(\omega) - \theta)$, as depicted in Figs. 9-11. The complete, numerically determined precursor structure that characterizes the electromagnetic impulse response of the four resonance Lorentz model of the frequency dispersion of the complex index of refraction of triply-distilled water, as given by Eq. (25) with the medium parameters listed in Table 1, is illustrated in the sequence of plots given in Fig. 12 at the fixed propagation distance $z = 6\pi \times 10^{-5}m$. The detailed analysis of the saddle point dynamics given in the preceding subsection is now used to explain each important feature observed in this

258

computed impulse response. Because of the exceptional quantitative agreement between the field structures depicted in Figs. 12(a)-(c) with their counterparts depicted in Fig. 4(a)-(c), this description also applies to the full model results obtained from Eq. (6) through intermediate values of the space-time parameter θ.

Over the initial space-time interval $\varepsilon_\infty^{1/2} < \theta < \theta_{SB_1}$, where $\theta_{SB_1} \cong 1.133$, the distant saddle point pair $SP_{5,6}$ is dominant and results in the asymptotic contribution

$$A(z,t) \sim \left(\frac{2c}{\pi z}\right)^{1/2} \Re\left\{ \left[-\phi''(\omega_5,\theta)\right]^{-1/2} e^{\frac{z}{c}\phi(\omega_5,\theta)} + \left[-\phi''(\omega_6,\theta)\right]^{-1/2} e^{\frac{z}{c}\phi(\omega_6,\theta)} \right\} \quad , \tag{27}$$

for $\varepsilon_\infty^{1/2} < \theta < \theta_{SB_1}$ as $z \to \infty$. This contribution yields the dynamical evolution of the Sommerfeld precursor field $A_S(z,t)$, whose front has an infinite instantaneous oscillation frequency and travels at the velocity $c/\varepsilon_\infty^{1/2}$, which is equal to the speed of light in vacuum for most (if not all) materials, including water[20]. As these distant saddle points move in from infinity and approach the branch points $\omega_{17_z}^\pm$ in the limit as $\theta \to \infty$, the attenuation $X(\omega_5,\theta)/c = X(\omega_6,\theta)/c$ increases so that the Sommerfeld precursor amplitude decreases monotonically, and the instantaneous frequency of oscillation $\omega_S(\theta) \cong \Re\{\omega_5(\theta)\}$ decreases monotonically from infinity and approaches the value $\Re\{\omega_{17_z}^+\}$ from above as $\theta \to \infty$, as seen in both Fig. 4(a) and Fig. 12(a).
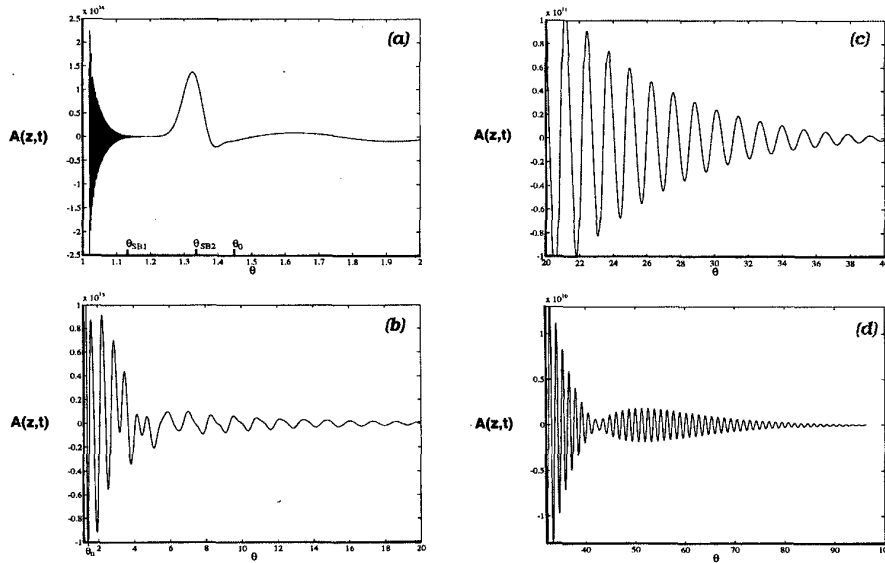

Figure 12. Dynamical evolution of the propagated field due to an input delta function pulse in the four resonance Lorentz model of triply-distilled water at the fixed propagation distance $z = 6\pi \times 10^{-5} m$ for small through large values of the space-time parameter $\theta = ct/z$.

Over the space-time interval $\theta_{SB_1} < \theta < \theta_{7,1}$, where $\theta_{7,1} \cong 1.3235$, the near saddle point SP_1 is dominant and results in the asymptotic contribution

$$A(z,t) \sim \left(\frac{c}{2\pi z}\right)^{\frac{1}{2}} \Re\left\{\left[-\phi''(\omega_1,\theta)\right]^{-\frac{1}{2}} e^{\frac{z}{c}\phi(\omega_1,\theta)}\right\} \quad , \quad \theta_{SB_1} < \theta < \theta_{7,1} \quad , \tag{28}$$

as $z \to \infty$, during which the propagated field is nonoscillatory (or quasi-static) and increases in amplitude as the dominant saddle point SP_1 moves down the positive imaginary axis with a resultant decreasing attenuation factor. Over the short space-time interval $\theta_{7,1} < \theta < \theta_{SB_2}$, where $\theta_{SB_2} \cong 1.359$, the pair of intermediate saddle points $SP_{7,8}$ become dominant and result in the asymptotic contribution

$$A(z,t) \sim \left(\frac{2c}{\pi z}\right)^{\frac{1}{2}} \Re\left\{\left[-\phi''(\omega_7,\theta)\right]^{-\frac{1}{2}} e^{\frac{z}{c}\phi(\omega_7,\theta)} + \left[-\phi''(\omega_8,\theta)\right]^{-\frac{1}{2}} e^{\frac{z}{c}\phi(\omega_8,\theta)}\right\} \quad , \tag{29}$$

for $\theta_{7,1} < \theta < \theta_{SB_2}$ as $z \to \infty$, which introduces a very brief oscillatory contribution with instantaneous frequency $\omega_I(\theta) \cong \Re\{\omega_7(\theta)\}$ to the propagated field. The first-order near saddle point SP_1 is again dominant over the space-time interval $\theta_{SB_2} < \theta < \theta_1$, where $\theta_1 \cong 1.51$, and results in the asymptotic contribution

$$A(z,t) \sim \left(\frac{c}{2\pi z}\right)^{\frac{1}{2}} \Re\left\{\left[-\phi''(\omega_1,\theta)\right]^{-\frac{1}{2}} e^{\frac{z}{c}\phi(\omega_1,\theta)}\right\} \quad , \quad \theta_{SB_2} < \theta < \theta_1 \quad , \tag{30}$$

as $z \to \infty$, during which the propagated field is quasi-static. At $\theta = \theta_0 = 1.49$, where $\theta_{SB_2} < \theta_0 < \theta_1$, $\phi(\omega_1(\theta_0),\theta_0) = 0$ and the asymptotic contribution (30) experiences no exponential decay, varying only as $z^{-\frac{1}{2}}$. As θ increases above θ_0 the exponential attenuation monotonically increases. Over the space-time interval $\theta_1 < \theta < \theta_{9,1}$, where $\theta_{9,1} \cong 1.71$, the near saddle point pair $SP_{1,15}$ is dominant and move apart symmetrically with respect to the imaginary axis, producing the asymptotic contribution

$$A(z,t) \sim \left(\frac{2c}{\pi z}\right)^{\frac{1}{2}} \Re\left\{\left[-\phi''(\omega_{15},\theta)\right]^{-\frac{1}{2}} e^{\frac{z}{c}\phi(\omega_{15},\theta)} + \left[-\phi''(\omega_1,\theta)\right]^{-\frac{1}{2}} e^{\frac{z}{c}\phi(\omega_1,\theta)}\right\} \quad , \tag{31}$$

for $\theta_1 < \theta < \theta_{9,1}$ as $z \to \infty$. The exponential attenuation of this field component increases monotonically with increasing θ, as seen in Fig. 8, while its instantaneous frequency of oscillation $\omega_I \cong \Re\{\omega_{15}(\theta)\}$ chirps upward from its quasi-static value at $\theta = \theta_1 \cong 1.51$ and approaches the limiting value $\Re\{\omega_{11_p}^+\}$ as $\theta \to \infty$. Over the space-time interval $\theta_{9,1} < \theta < \theta_{13,9}$, where $\theta_{9,1} \cong 1.71$ and $\theta_{13,9} \cong 1.73$ for triply-distilled water, the middle saddle point pair $SP_{9,10}$ is dominant and produces the asymptotic contribution

$$A(z,t) \sim \left(\frac{2c}{\pi z}\right)^{\frac{1}{2}} \Re\left\{\left[-\phi''(\omega_9,\theta)\right]^{-\frac{1}{2}} e^{\frac{z}{c}\phi(\omega_9,\theta)} + \left[-\phi''(\omega_{10},\theta)\right]^{-\frac{1}{2}} e^{\frac{z}{c}\phi(\omega_{10},\theta)}\right\} \quad , \tag{32}$$

260

for $\theta_{9,1} < \theta < \theta_{13,9}$ as $z \to \infty$, whose instantaneous frequency of oscillation $\omega_I \cong \Re\{\omega_9(\theta)\}$ chirps downwards towards the value $\Re\{\omega_{13_z}^+\}$ in the limit as $\theta \to \infty$. Finally, the first-order saddle point pair $SP_{13,14}$ are dominant for all $\theta > \theta_{13,9}$ and produce the asymptotic contribution

$$A(z,t) \sim \left(\frac{2c}{\pi z}\right)^{\frac{1}{2}} \Re\left\{ \left[-\phi''(\omega_{13},\theta)\right]^{-\frac{1}{2}} e^{\frac{z}{c}\phi(\omega_{13},\theta)} + \left[-\phi''(\omega_{14},\theta)\right]^{-\frac{1}{2}} e^{\frac{z}{c}\phi(\omega_{14},\theta)} \right\} \quad , \tag{33}$$

for $\theta_{13,9} < \theta$, as $z \to \infty$, whose instantaneous frequency of oscillation $\omega_I \cong \Re\{\omega_{13}(\theta)\}$ chirps upwards and approaches the value $\Re\{\omega_{13_p}^+\}$ as $\theta \to \infty$.

The set of expressions given in Eqs. (28)-(33) yields the dynamical evolution of the Brillouin precursor field $A_B(z,t)$. The initial behavior of this precursor field is dominated by the asymptotic contribution due to the first-order saddle point SP_I which results in the quasi-static growth of this field, where the field amplitude at the critical space-time point $\theta = \theta_0$ decays only algebraically as $z^{-\frac{1}{2}}$. However, due to interference with the contributions from the two saddle point pairs $SP_{7,8}$ and $SP_{13,14}$, the observed amplitude peak in the Brillouin precursor field is shifted towards an earlier space-time point just prior to the value θ_{SB_2}, as seen in Fig. 12(a). As the propagation distance increases, this amplitude peak shifts upwards and approaches the critical value θ_0 from below in the limit as $z \to \infty$. The velocity of this peak in the Brillouin precursor then slows down from its initial value c/θ_{SB_2} and approaches the value c/θ_0 as the propagation distance increases.

As θ increases above θ_1 the propagated field is initially dominated by the asymptotic contribution due to the saddle point pair $SP_{1,15}$ which results in an increasingly attenuated field with an upwardly chirping instantaneous angular frequency of oscillation. For all $\theta > \theta_{9,1}$ the propagated field is dominated by the asymptotic contributions due to the two pairs of saddle points $SP_{9,10}$ and $SP_{13,14}$, which possess nearly equal attenuation over this entire space-time domain. Because of their different instantaneous oscillation frequencies, their superposition then results in the observed quenching of the oscillatory relaxation of the Brillouin precursor and the resultant beat structure over the space-time domain $\theta > \theta_{9,1}$ that is clearly evident in both Figs. 4 and 12.

DISCUSSION

The electromagnetic impulse response of the full Rocard-Powles-Lorentz model for the frequency dispersion of the dielectric permittivity of triply-distilled water with two relaxation times and four resonance lines, depicted in Fig. 4, displays the complete Sommerfeld precursor field structure followed by a Brillouin precursor field structure whose oscillatory relaxation is quenched. Each of the predominant features observed in this propagated field is completely explained by the four resonance Lorentz model (depicted in Fig. 12) with the single exception of the long-time exponential relaxation observed in Fig. 4 for the full model. It is quite surprising that the effects of rotational polarization, which dominate the observed frequency dispersion depicted in Figs. 1-2, have only a minor effect on the propagated field. In particular, one might expect that the quasi-static peak in the Brillouin precursor would occur at the

space-time point $\theta = n(0) \cong 8.902$ that is a characteristic of the rotational polarization component when the full model is used, and not at the space-time point $\theta_0 = n(0) \cong 1.501$ that is predicted by the quartic resonance Lorentz model given in Eq. (25). However, the latter result is correct while the former is not even close. This surprising result, together with the quenched oscillatory and long-time exponential relaxation of the Brillouin precursor field demonstrate intriguing interactions between the rotational and resonance components of the Rocard-Powles-Lorentz model considered here.

Table 1. Optimized parameter values for the Rocard-Powles-Lorentz model for the frequency dispersion of the dielectric permittivity of triply-distilled water.

$$\varepsilon_\infty = 1$$

Rocard-Powles Model Parameters

(Microwave Region)

$a_0 = 74.1$	$\tau_0 = 8.44 \times 10^{-12} s$	$\tau_{f0} = 4.93 \times 10^{-14} s$
$a_2 = 2.90$	$\tau_2 = 6.05 \times 10^{-14} s$	$\tau_{f2} = 8.59 \times 10^{-15} s$

Lorentz Model Parameters

(Infrared Region)

$\omega_{11}/2\pi = 1.8 \times 10^{13} Hz$	$b_{11}/2\pi = 1.2 \times 10^{13} Hz$	$\delta_{11}/2\pi = 4.3 \times 10^{12} Hz$
$\omega_{13}/2\pi = 4.9 \times 10^{13} Hz$	$b_{13}/2\pi = 6.8 \times 10^{12} Hz$	$\delta_{13}/2\pi = 8.4 \times 10^{11} Hz$
$\omega_{15}/2\pi = 1.0 \times 10^{14} Hz$	$b_{15}/2\pi = 2.0 \times 10^{13} Hz$	$\delta_{15}/2\pi = 2.8 \times 10^{12} Hz$

(Ultraviolet Region)

$\omega_{17}/2\pi = 3.7 \times 10^{15} Hz$	$b_{17}/2\pi = 3.2 \times 10^{15} Hz$	$\delta_{17}/2\pi = 8.0 \times 10^{14} Hz$

REFERENCES

1. J. Jones, On the propagation of a pulse through a dispersive medium, Am. J. Phys. 42:43 (1974).
2. D. G. Anderson and J. I. H. Askne, Wave packets in strongly dispersive media, Proc. IEEE 62:1518 (1974).
3. D. Anderson, J. Askne, and M. Lisak, Wave packets in an absorbing and strongly dispersive medium, Phys. Rev. A 12:1546 (1975).
4. I. P. Christov, Generation and propagation of ultrashort optical pulses, in: "Progress in Optics," vol. XXIX, E. Wolf, ed., Elsevier, Amsterdam (1991), pp. 199-291.
5. K. E. Oughstun and C. M. Balictsis, Gaussian pulse propagation in a dispersive, absorbing dielectric, Phys. Rev. Lett. 77:2210 (1996).
6. K. E. Oughstun and H. Xiao, Failure of the quasimonochromatic approximation for ultrashort pulse propagation in a dispersive, attenuative medium, Phys. Rev. Lett. 78:642 (1997).
7. A. Sommerfeld, Über die fortpflanzung des lichtes in disperdierenden medien, Ann. Phys. 44:177 (1914).
8. L. Brillouin, Über die fortpflanzung des licht in disperdierenden medien, Ann. Phys. 44:203 (1914).
9. L. Brillouin. "Wave Propagation and Group Velocity," Academic, New York (1960).
10. P. Debye, Näherungsformeln für die zylinderfunktionen für grosse werte des arguments und unbeschränkt verander liche werte des index, Math. Anal. 67:535 (1909).
11. K. E. Oughstun and G. C. Sherman, Propagation of electromagnetic pulses in a linear dispersive medium with absorption (the Lorentz medium), J. Opt. Soc. Am. B 5:817 (1988).
12. K. E. Oughstun and G. C. Sherman, Uniform asymptotic description of electromagnetic pulse propagation in a linear dispersive medium with absorption (the Lorentz medium), J. Opt. Soc. Am. A 6:1394 (1989).
13. K. E. Oughstun and G. C. Sherman, Asymptotic theory of pulse propagation in absorbing and dispersive dielectrics, in: "Review of Radio Science, 1990-1992," W. R. Stone, ed., Oxford (1993), pp. 75-105.
14. K. E. Oughstun and G. C. Sherman. "Electromagnetic Pulse Propagation in Causal Dielectrics," Springer-Verlag, Berlin (1994).
15. F. W. J. Olver, Why steepest descents?, SIAM Rev. 12:228 (1970).
16. K. Moten, C. Durney, and T. Stockham, Jr., Electromagnetic pulse propagation in dispersive planar dielectrics, Bioelectromagnetics 10:35 (1989).
17. K. Moten, C. Durney, and T. Stockham, Jr., Electromagnetic pulsed-wave radiation in spherical models of dispersive biological substances, Bioelectromagnetics 12:319 (1991).
18. R. Albanese, J. Penn, and R. Medina, Short rise-time microwave pulse propagation through dispersive biological media, J. Opt. Soc. Am. A 6:1441 (1989).
19. K. E. Oughstun, J. E. K. Laurens, and C. M. Balictsis, Asymptotic description of electromagnetic pulse propagation in a linear dispersive medium, in: "Ultra-Wideband, Short-Pulse Electromagnetics," L. Carin and L. B. Felsen, eds., Plenum, New York (1993), pp. 223-240.
20. K. E. Oughstun, Dynamical structure of the precursor fields in linear dispersive pulse propagation in lossy dielectrics, in: "Ultra-Wideband, Short-Pulse Electromagnetics 2," L. Carin and L. B. Felsen, eds., Plenum, New York (1995), pp. 257-272.
21. P. D. Smith and K. E. Oughstun, Electromagnetic energy dissipation of ultrawideband plane wave pulses in a causal, dispersive dielectric, in:

"Ultra-Wideband, Short-Pulse Electromagnetics 2," L. Carin and L. B. Felsen, eds., Plenum, New York (1995), pp. 285-295.

22. K. E. Oughstun, Noninstantaneous, finite rise-time effects on the precursor field formation in linear dispersive pulse propagation, J. Opt. Soc. Am. A 12:1715 (1995).

23. R. Albanese, J. Blaschak, R. Medina, and J, Penn, Ultrashort electromagnetic signals: biophysical questions, safety issues, and medical opportunities, Aviat. Space Environ. Med. 65:116 (1994).

24. S. Shen and K. E. Oughstun, Dispersive pulse propagation in a double resonance Lorentz medium, J. Opt. Soc. Am. B 6:948 (1989).

25. J. E. K. Laurens. "Plane Wave Pulse Propagation in a Linear, Causally Dispersive Polar Medium," Ph.D. Dissertation, University of Vermont, 1993.

26. C. F. Bohren and D. R. Huffman. "Absorption and Scattering of Light by Small Particles," Wiley, New York (1983), ch. 9.

27. J. McConnell," Rotational Brownian Motion and Dielectric Theory," Academic, London (1980).

28. P. Debye. "Polar Molecules," Dover, New York (1929).

29. C. J. F. Böttcher and A. Bordewijk. "Theory of Electric Polarization," vol. 2, Elsevier, Amsterdam (1980).

30. H. A. Lorentz. "The Theory of Electrons," Dover, New York (1952).

31. L. Rosenfeld. "Theory of Electrons," Dover, New York (1965).

32. H. J. Liebe, G. A. Hufford, and T. Manabe, A model for the complex permittivity of water at frequencies below 1 Thz, Int. J. Infrared and Millimeter Waves 12:659 (1991).

33. P. Wyns, D. P. Foty, and K. E. Oughstun, Numerical analysis of the precursor fields in linear dispersive pulse propagation, J. Opt. Soc. Am. A 6:1421 (1989).